

# Idealized Particle-Resolved Large-Eddy Simulations to Evaluate the Impact of Emissions Spatial Heterogeneity on CCN Activity

Samuel Frederick<sup>1</sup>, Matin Mohebalhojeh<sup>2</sup>, Jeffrey Curtis<sup>1,2</sup>, Matthew West<sup>2</sup>, and Nicole Riemer<sup>1</sup>

<sup>1</sup>Department of Climate, Meteorology, and Atmospheric Sciences, University of Illinois Urbana–Champaign, 1301 W. Green St., Urbana, IL 61801, USA

<sup>2</sup>Department of Mechanical Science and Engineering, University of Illinois Urbana–Champaign, 1206 W. Green St., Urbana, IL, 61801, USA

**Correspondence:** Nicole Riemer (nriemer@illinois.edu)

**Abstract.** Aerosol-cloud interactions remain a large source of uncertainty in global climate models (GCMs) due to complex, non-linear processes that alter aerosol properties and the inability to represent the full compositional complexity of aerosol populations within large-scale modeling frameworks. The spatial resolution of GCMs is often coarser than the scale of the spatially varying emissions in the modeled geographic region. This results in diffuse, uniform concentration fields of primary aerosol 5 and gas-phase species instead of spatially heterogeneous concentrations. Aerosol processes such as gas-particle partitioning and coagulation are concentration-dependent in a non-linear manner, and thus the representation of spatially heterogeneous emissions impacts aerosol aging and properties. This includes climate-relevant quantities key to aerosol-cloud interactions including particle hygroscopicity and cloud condensation nuclei (CCN) activity. We investigate the impact of emissions spatial 10 heterogeneity on aerosol properties including CCN activity via a series of first-of-a-kind particle-resolved large-eddy simulations with the modeling framework WRF-PartMC-MOSAIC-LES. CCN concentrations within the planetary boundary layer (PBL) are compared across numerous scenarios ranging in emissions spatial heterogeneity. We find that CCN concentrations at low supersaturations ( $S = 0.1\text{--}0.3\%$ ) increase in the upper PBL by up to 25% for emissions scenarios with high spatial heterogeneity when compared to a uniform emissions base case. Process level analysis indicates that this increase is due to enhanced nitrate formation among scenarios with high emissions spatial heterogeneity.

## 15 1 Introduction

Aerosols are known to impose a net negative radiative forcing, however considerable uncertainty persists in the representation of radiative forcing due to aerosol-cloud interactions (ACI) (Forster et al., 2021). Advancements in computing power have allowed modelers to investigate key contributing factors which alter the intensity of radiative forcing due to ACI such as spatial resolution (Ma et al., 2015). Simultaneously, improvements in computational power have advanced the representation 20 of aerosols in climate models through inclusion of more complex chemical mechanisms (Zaveri et al., 2021) and detailed aerosol treatments such as the Community Aerosol and Radiation Model for Atmospheres (CARMA), which is a 40 bin sectional model used by the Community Earth System Model 2 (CESM2) (Tilmes et al., 2023) and has shown improvements in representing aerosol properties when compared to the 4 bin Modal Aerosol Model (MAM4). While these two key structural

components to models—the treatment of aerosols and the effect of spatial resolution—have improved representation of aerosols and their radiative forcing, these aspects have yet to be explored in tandem to investigate the role of spatial heterogeneities typically below the grid scale of current climate models alongside detailed aerosol treatments in modifying the depiction of climate-relevant aerosol properties key to ACI such as cloud condensation nuclei (CCN) activity.

Aerosol-aware climate models typically contain a sub-model which governs the aerosol representation and associated processes. Given computational constraints, the aerosol treatment is often highly simplified with regard to aerosol compositional diversity. For instance, E3SM uses the modal aerosol model MAM4 which contains four lognormally distributed modes (Golaz et al., 2022). Such a treatment constrains the diversity of the aerosol population to four internally-mixed modes (i.e., all particles within a mode are compositionally identical). As a result, modal and sectional aerosol treatments underrepresent the true compositional complexity of an aerosol population in which each particle ages independently. Particle-resolved aerosol models allow representation of the full compositional diversity of an aerosol population via a set of computational particles which are allowed to compositionally vary and age independently. Particle resolved models such as the Particle Monte Carlo model (PartMC) have been used extensively to investigate the sensitivity of CCN activity to the composition of emitted aerosol particles (Fierce et al., 2013), aging timescales due to condensation and coagulation for carbonaceous CCN (Fierce et al., 2015), and the sensitivity of CCN estimates to mixing state (i.e., the compositional diversity within and across aerosols) (Ching et al., 2017). Furthermore, given that a particle-resolved model can fully represent aerosol composition space, PartMC has been used to estimate error in CCN activity for coarser aerosol treatments by comparing depicted CCN concentrations against compositionally-averaged output reminiscent of a sectional or modal model (Zaveri et al., 2010; Ching et al., 2017). Furthermore, direct comparison of CCN activity depicted by PartMC and MAM4 has shown considerable divergence, especially in polluted regions where high rates of coagulation and gas-particle partitioning amplify model disagreement (Fierce et al., 2024).

In addition to the treatment of aerosols, the depiction of spatial heterogeneity—including that of surface properties, emissions of gas phase species and primary aerosol, and heterogeneous distributions of their resulting plumes— influences particle aging and associated properties including CCN activity. Present aerosol-aware models at regional and global scales possess insufficient resolution to capture the full spatial heterogeneity of aerosols and the emissions of primary aerosols and gas phase precursors. In turn, these models depict artificially dilute and uniform concentrations within grid cells. This alters the representation of concentration-dependent, non-linear aerosol processes such as coagulation and gas particle partitioning. Past studies have shown that climate-relevant aerosol properties such as aerosol optical properties (Gustafson Jr. et al., 2011) and CCN activity (Weigum et al., 2016) are highly sensitive to the model’s grid resolution with a large contribution of sub-grid scale variability resulting from the spatially varying pattern of emissions (Qian et al., 2010).

Past studies evaluating the sub-grid variability of aerosol properties often compare outputs from models with coarse resolution typical of global climate models ( $\sim 50\text{--}100$  km) against higher resolution model outputs with resolution on the order of  $\sim 1\text{--}10$  km (Qian et al., 2010; Gustafson Jr. et al., 2011; Weigum et al., 2016; Crippa et al., 2017; Lin et al., 2017). While such improvements in resolution better resolve heterogeneities in emissions, there still exists considerable unresolved spatial

heterogeneity in the sub-kilometer scale. In addition, such modeling studies do not explicitly resolve the scales of turbulent transport in the boundary layer, instead fully parameterizing turbulence via Reynolds-averaged Navier Stokes.

60 The evolution of emission plumes containing gas phase compounds and aerosols is highly dependent on turbulent mixing at fine spatial scales and the proximity of reactive species. A considerable body of literature has investigated the role of turbulence-chemistry interactions and chemical segregation on gas phase reactions in the planetary boundary layer via the use of large-eddy simulations (LES). Brasseur et al. (2023) review recent applications of LES to investigate chemical segregation and turbulence chemistry interactions in a variety of spatially heterogeneous geographic regions. Past studies tend to focus on the oxidation of  
65 highly reactive volatile organic compounds (VOCs) such as isoprene and have shown that spatially heterogeneous emissions contribute to the chemical segregation between reactive gas phase species in the boundary layer (Ouwersloot et al., 2011; Kaser et al., 2015). Note, however, that these studies do not model aerosols, although the coupling between the gas phase and aerosols through gas-particle partitioning suggests chemical segregation due to the spatial heterogeneity of emissions likely influences the aerosol state.

70 Recently, numerous turbulence-resolving frameworks have been coupled to aerosol models including the use of the Sectional Aerosol model for Large Scale Applications (SALSA) (Kokkola et al., 2008) alongside UCLALES (Tonttila et al., 2017) and the Parallelized Large-Eddy Simulation Model (PALM) (Kurppa et al., 2019) as well as the coupling between the modal model M7 (Vignati et al., 2004) and the Dutch Atmospheric Large-Eddy Simulation model (DALES) (de Bruine et al., 2019). Although these models have high-resolution transport schemes, they each possess relatively coarse-resolution aerosol treatments.  
75 For instance, UCLALES-SALSA uses a 10-bin sectional treatment while DALES implements a modified version of the seven-mode M7 model to allow two additional hydrometeor modes. To our knowledge, no aerosol-aware transport model has yet to leverage a high-resolution particle resolved aerosol treatment alongside turbulence resolving transport frameworks such as LES.

The aim of this work is to conduct a process-level analysis of the complex coupling between the spatial heterogeneity  
80 of surface emissions (including both gas compounds and primary aerosol), aerosol aging processes, and the resulting impact on aerosol properties including CCN activity via a set of first-of-a-kind particle-resolved LES. This establishes a high resolution aerosol-transport model framework in both explicit representation of turbulent transport as well as aerosol composition, properties, and aging.

This paper is organized in the following manner. Section 2 presents the modeling framework used in this study, WRF-  
85 PartMC-MOSAIC-LES, alongside a description of numerous emissions scenarios ranging in spatial heterogeneity. Section 3 discusses results of simulation runs, and a description of changes to the aerosol size distribution, composition, hygroscopicity, and CCN activity across emissions scenarios are discussed. We conclude with remarks on the implications of this study, limitations stemming from its idealized nature, and future work.

## 2 Methods

### 90 2.1 WRF-PartMC-MOSAIC-LES

The aerosol-transport model WRF-PartMC-MOSAIC-LES is a coupling of numerous sub-models responsible for transport, the aerosol representation, and multiphase chemistry. WRF-PartMC-MOSAIC-LES is an extension of the aerosol-transport model WRF-PartMC, which was developed by Curtis et al. (2017) for particle diffusion and recently extended to include advection (Curtis et al., 2024). WRF-PartMC couples the Weather Research and Forecasting model (WRF) (Skamarock et al., 2008) and 95 the particle-resolved aerosol model PartMC (Riemer et al., 2009). PartMC represents a population of aerosol particles using an ensemble of computational particles, each with appropriate weighting (i.e., particle multiplicity) to represent the diversity of particle sizes and composition apparent in actual aerosol populations. The composition of each computational particle is allowed to vary as particles age. PartMC is a box model, meaning that the relative position of particles within computational grid cells is not tracked. Instead, the transport of particles into and out of grid cells is handled by a stochastic advection 100 algorithm housed in the interface between PartMC and the dynamical model WRF (Curtis et al., 2024). WRF-PartMC has been used in a 1-dimensional setting to resolve vertical gradients in aerosol composition and mixing state (Curtis et al., 2017) and more recently in a 3-dimensional setting to illustrate transport of particles by simulated meteorology over a regional domain (Curtis et al., 2024).

LES models explicitly resolve large scales of turbulent motion; however, they must parameterize eddies which cannot be 105 resolved below the grid resolution on the order of 10–100 m and the down-gradient tendency of turbulent kinetic energy (TKE) to be transferred from large to small scales, ultimately dissipating as heat energy. This requires use of closure schemes, and WRF-PartMC-MOSAIC-LES utilizes Deardorff's TKE scheme for eddy diffusivity and eddy viscosity parameterizations (Deardorff, 1980).

Both gas-phase and aerosol chemistry are represented using the Model for Simulating Aerosol Interactions and Chemistry 110 (MOSAIC) (Zaveri et al., 2008). MOSAIC is comprised of numerous sub-models, including the Carbon Bond Mechanism version Z (CBM-Z) which solves gas phase chemistry (Zaveri and Peters, 1999). Phase-dependent partitioning of aerosol species is handled by the Multicomponent Equilibrium Solver for Aerosols (MESA) (Zaveri et al., 2005a). Activity coefficients of electrolytes are parameterized via the multicomponent Taylor expansion method (MTEM) (Zaveri et al., 2005b). In order to solve the numerically stiff set of solid-liquid phase reactions governing thermodynamic equilibrium, MOSAIC utilizes the 115 adaptive step time-split Euler method (ASTEM) (Zaveri et al., 2008). MOSAIC models aerosol chemistry for both inorganic and organic compounds such as nitrate, ammonium, sulfate, black carbon (BC), and a limited set of secondary organic aerosol (SOA) species.

### 2.2 Computational domain setup

The computational domain has a horizontal extent of 10 km in both  $x$ - and  $y$ -axes, with horizontal grid spacing of 100 m. In the 120 vertical, the domain extends to 2 km and is represented with 200 vertical levels. WRF uses an  $\eta$  vertical coordinate system and for LES runs, vertical levels are linearly spaced in pressure. This results in an effective vertical grid spacing of approximately

10 m. Simulations are configured to begin on the Vernal Equinox at 09:00 local time and conclude at 15:00 for a total duration of 6 hours in order to balance photolysis rates throughout simulations. Each grid cell is initialized with 100 computational particles, resulting in 100 million total particles. As processes such as emission, transport, and coagulation alter the number concentration of particles within grid cells, the number of computational particles is kept near the initial value by doubling (halving) the number of computational particles in a grid cell once the number is half (twice) the initial value.

The surface of the domain is characterized by a uniform, flat surface absent of topographical features or land-use variations. Note that WRF-PartMC-MOSAIC-LES is not coupled to one of WRF's radiation sub-models. Instead, MOSAIC utilizes idealized parameterizations to determine photolysis rates based on the solar zenith angle. Due to the lack of a radiation sub-130 model, surface heating is imposed uniformly across the domain using a constant rate of  $0.24 \text{ K m}^{-1} \text{ s}^{-1}$ .

Both aerosol and gas phase initial conditions and emissions are chosen to represent species and concentrations typical of an urban plume and are adopted from Riemer et al. (2009). Initial concentrations and emission rates were adapted from the 1987 Southern California Air Quality Study (SCAQS) during which measurements of gas phase species and particulate matter mass concentrations were collected at multiple sites across the Los Angeles basin (Zaveri et al., 2008). Table 1 contains initial 135 concentrations and emission rates for gas phase species. Table 2 includes aerosol initial conditions and emission rates organized by aerosol modes. Initially, the aerosol is an equal mixture of ammonium sulfate and primary organic aerosol (POA). The three emission modes including cooking and vehicular combustion are varied mixtures of POA and BC. To allow for simulation spin-up during which time the convective boundary layer fully develops, all emission rates are set to zero during the first hour of simulations. Subsequently, emitted compounds are released at the surface at constant rates indicated by Tables 1 and 2 for 140 the remainder of simulations.

Meteorological initial conditions are specified using an idealized sounding for a convective boundary layer where the surface is 5 K warmer than the mixing layer and is capped by an inversion of 8 K at 1 km. The wind profile is zero throughout the entire vertical extent of the domain.

### 2.3 Emissions Scenarios

145 We evaluate the impacts of emissions spatial heterogeneity on aerosol properties via numerous emissions scenarios shown in Figure 1. Emissions are first released uniformly over the entire domain. This scenario, referred to as the uniform base case, serves as a proxy for coarser resolution models which do not resolve the spatial heterogeneity of emissions and instead emit gas compounds and primary aerosol in a uniform and diffuse manner across grid cells. Successive scenarios are compared against this uniform base case to evaluate modifications to aerosol properties resulting from the spatial heterogeneity of emissions. 150 Scenario 1 represents an idealized depiction of an urban-rural interface, whereby emissions are released in half the domain with no emissions occurring in the other half. Scenario 2 contains a narrow strip of emissions running through the center of the domain, corresponding to an emission pattern typical of a busy roadway. Lastly, scenario 3 places all emissions in a single grid cell in the center of the domain and is representative of a point-source emission, such as a plume from an industrial source.

Emissions scenarios are chosen to represent a range of spatial heterogeneity, which is quantified using the metric  $\eta$  developed 155 by (Mohebalhojeh et al., 2024) make sure to update this citation when Matin's paper is published.  $\eta$  is a normalized measure

**Table 1.** Gas phase emissions and initial conditions. Table adapted from Riemer et al. (2009) with permission.

Species	Symbol	Initial Mole Fraction (ppb)	Emissions (nmol m <sup>-2</sup> s <sup>-1</sup> )
Nitric oxide	NO	0.1	31.8
Nitrogen dioxide	NO <sub>2</sub>	1.0	1.67
Nitric acid	HNO <sub>3</sub>	1.0	
Ozone	O <sub>3</sub>	50.0	
Hydrogen peroxide	H <sub>2</sub> O <sub>2</sub>	1.1	
Carbon monoxide	CO	21	291.3
Sulfur dioxide	SO <sub>2</sub>	0.8	2.51
Ammonia	NH <sub>3</sub>	0.5	6.11
Hydrogen chloride	HCl	0.7	
Methane	CH <sub>4</sub>	2200	
Ethane	C <sub>2</sub> H <sub>6</sub>	1.0	
Formaldehyde	HCHO	1.2	1.68
Methanol	CH <sub>3</sub> OH	0.12	0.28
Methyl hydrogen peroxide	CH <sub>3</sub> OOH	0.5	
Acetaldehyde	ALD2	1.0	0.68
Paraffin carbon	PAR	2.0	96
Acetone	AONE	1.0	1.23
Ethene	ETH	0.2	7.2
Terminal olefin carbons	OLET	$2.3 \cdot 10^{-2}$	2.42
Internal olefin carbons	OLEI	$3.1 \cdot 10^{-4}$	2.42
Toluene	TOL	0.1	4.04
Xylene	XYL	0.1	2.41
Lumped organic nitrate	ONIT	0.1	
Peroxyacetyl nitrate	PAN	0.8	
Higher organic acid	RCOOH	0.2	
Higher organic peroxide	ROOH	$2.5 \cdot 10^{-2}$	
Isoprene	ISOP	0.5	0.23
Alcohols	ANOL		3.45

of spatial heterogeneity, ranging from 0 (fully homogeneous) to 1 (fully heterogeneous). For a discrete 2-dimensional scalar field  $f$  defined over a domain  $S$  with dimensions  $N$  by  $M$ ,  $\eta$  is defined as

**Table 2.** Aerosol emissions and initial conditions. Table adapted from Riemer et al. (2009) with permission.

Initial/Background	$N$ ( $\text{m}^{-3}$ )	$D_{\text{gn}}$ ( $\mu\text{m}$ )	$\sigma_g$	Composition by Mass
Aitken Mode	$3.2 \cdot 10^9$	0.02	1.45	50% $(\text{NH}_4)_2\text{SO}_4$ , 50% POA
Accumulation Mode	$2.9 \cdot 10^9$	0.116	1.65	50% $(\text{NH}_4)_2\text{SO}_4$ , 50% POA
Emissions	$E$ ( $\text{m}^{-2} \text{s}^{-1}$ )	$D_{\text{gn}}$ ( $\mu\text{m}$ )	$\sigma_g$	Composition by Mass
Meat cooking	$9 \cdot 10^6$	0.086	1.9	100% POA
Diesel vehicles	$1.6 \cdot 10^8$	0.05	1.7	30% POA, 70% BC
Gasoline vehicles	$5 \cdot 10^7$	0.05	1.7	80% POA, 20% BC

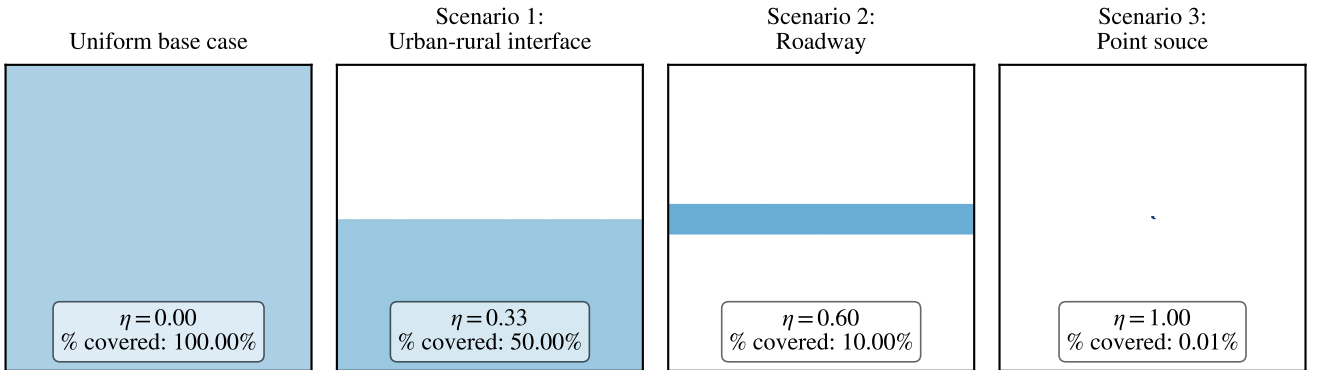


**Figure 1.** Emissions spatial heterogeneity scenarios. The pattern of emissions is shown as a cross section of the x-y plane at ground level. Shaded areas correspond to regions of emissions. The hue of shading indicates the intensity of emissions scaling ranging from light blue (low emissions scaling) to dark blue (high emissions scaling). Both the spatial heterogeneity metric  $\eta$  and the fraction of area covered by emissions are displayed in the bottom of each scenario.

$$\eta(f, S) = \frac{\sum_{\tilde{S} \in \mathbb{R}} |\bar{f}(S) - \bar{f}(\tilde{S})|}{\bar{f}(S) [\frac{3}{2}(N \times M)(N-1)(M-1) + N(N-1) + M(M-1)]}, \quad (1)$$

where  $\bar{f}(S)$  is the domain mean and  $\bar{f}(\tilde{S})$  is the mean over a subset of the domain  $\tilde{S}$ . Thus, the metric is computed by summing the absolute value of the difference between the domain mean  $\bar{f}(S)$  and all domain subset means  $\bar{f}(\tilde{S})$ , normalized by the product of the domain mean and the number of possible subsets. Mohebalhojeh et al. (2024) show that the metric is translationally invariant when the scalar field  $f$  is translated over the domain  $S$ . Furthermore, it is presented in theorem

and proof that the maximum spatial heterogeneity over a discrete domain occurs when the value of the scalar field is zero everywhere except at a single point at which it takes the value  $MN \times \bar{f}(S)$ .

165 Thus, the uniform base case corresponds to the homogeneous condition while scenario 3—a point source emission in which all emissions are released from a grid cell in the center of the domain—represents the maximally heterogeneous emissions scenario. To ensure the mass of gas species and aerosol emitted per unit of time is consistent across each scenario, emission rates are divided by the fraction of area covered by emissions. For instance, in scenario 3, this results in a scaling of 10,000 ( $M = N = 100$ ) for the point-source emission. The fraction of area covered by emissions is displayed for each scenario alongside the  
170 spatial heterogeneity as quantified via the metric of Mohebalhojeh et al. (2024) in Figure 1.

### 3 Results

Key findings of this paper are structured in the following manner. Section 3.1 investigates the coupling between emissions spatial heterogeneity and the gas phase. In Section 3.2, impacts of emissions spatial heterogeneity on bulk aerosol properties (number and mass concentrations) are presented. Impacts on aerosol composition are then presented in Section 3.3 with particular focus on sulfur, ammonium, and nitrate, as these compounds largely influence a particles hygroscopicity. Leveraging the particle-resolved framework, we evaluate how particle hygroscopicity responds to emissions spatial heterogeneity via 2-dimensional particle distributions. Having systematically explored impacts of emissions spatial heterogeneity on the aerosol state, Section 3.4 investigates impacts on CCN activity at numerous supersaturation levels ranging from 0.1% to 1.0%. Lastly, we explore the impact of two key factors that govern the impact of emissions spatial heterogeneity on CCN activity. Namely, we  
175 investigate impacts of aerosol composition—in particular, the presence of ammonia—and mean wind in the planetary boundary layer in Sections 3.5 and 3.6, respectively.  
180

#### 3.1 Impacts of emissions spatial heterogeneity on gas phase species

Figure 2 displays cross sections in the x-y plane of ammonia, nitric acid, and the hydroxyl radical (OH) at  $t = 6$  h. Cross sections indicate the spatial organization of each gas phase compound in the upper boundary layer at  $z \approx 900$  m. Cross sections are organized by species along columns and by emissions scenario along rows. The spatial heterogeneity  $\eta$  of each cross section  
185 is shown at the top of each subplot. The concentration of compounds in each cross section is indicated by colored shading, ranging from dark blue (low concentrations) to yellow (high concentrations). Note that in order to illustrate the structure of each cross section, the coloring does not indicate the absolute magnitude of a given species concentration as the absolute difference between, for instance, ammonia concentrations near the emission plume and OH concentrations span orders of magnitude.  
190 Instead, the colored shading of each cross section is normalized relative to the range of concentrations observed.

The spatial heterogeneity of ammonia is consistently 3–4 times higher than both nitric acid and OH. This is primarily due to the fact that ammonia is emitted while nitric acid and OH are formed due to chemical reactions. The similar structure between ammonia and nitric acid indicates that nitric acid formation is most effective over the emissions plume due to the emission of NO and  $\text{NO}_2$ . The spatial pattern of OH mirrors ammonia and nitric acid, with lower concentrations near the center of

195 the emissions plume and higher concentrations farther away. This indicates the rapid oxidation of many reactive compounds occurring in the emissions plume. Notably, this illustrates how OH becomes spatially segregated from its reactants in the emissions plume as OH in the immediate vicinity of the plume is reacted away.

Figure 3 shows vertical profiles of gas phase concentrations for ammonia, nitric acid, and OH. For ammonia and nitric acid, the horizontal average across the domain is shown at each vertical level. Averaging over the entire domain, both ammonia and 200 nitric acid concentrations decrease as spatial heterogeneity increases. As will be shown in Section 3.3, this is due to increased partitioning of ammonia and nitric acid into the aerosol phase to form ammonium nitrate.

Because OH concentrations are reduced in the vicinity of the emissions plume as shown in Figure 2, the value of the 5th percentile within each vertical level is shown in Figure 3. Scenarios with high emissions spatial heterogeneity indicate a significant reduction in OH near the emissions plume. Whereas in the uniform base case, the level-mean concentration of OH 205 is 0.61 pptv at  $z = 1$  km, OH is reduced by 54% to 0.28 pptv for scenario 3.

### 3.2 Aerosol size distributions

Number and mass distributions for each emissions scenario are shown in Figure 4. The initial condition corresponds to the black dashed line, indicating a bimodal distribution of Aitken and accumulation mode particles. Solid lines indicate the distribution at the end of each simulation ( $t = 6$  h). The uniform base case corresponds to the solid black line, where emissions 210 scenarios are indicated by colored solid lines. Each size distribution is taken from a vertical level in the upper boundary layer at  $z \approx 800$  m. Due to the stochastic treatment of aerosol particles in WRF-PartMC and the selected number of computational particles per grid cell ( $N = 100$ ), both number and mass distributions represent the average distribution in a  $1 \text{ km}^2$  region centered over the emissions plume (i.e., size distributions are averaged over a  $10 \times 10$  grid cell region). For the uniform base case, scenario 2 and scenario 3, this region is directly over the center of the domain. For scenario 1, emissions are released in 215 one half of the domain that is offset from the center, and thus the averaging region is located in the center of the emissions patch. For each size distribution, data have been binned into 100 bins, ranging in size from  $10^{-9}$  to  $10^{-3}$  m.

Separating the size distribution into Aitken ( $D_p < 50$  nm) and accumulation ( $D_p < 50$  nm) modes, the total number and mass concentration was calculated for each mode. As the spatial heterogeneity of emissions increases from the uniform base case to scenario 3, we find that the number of Aitken mode particles decreases by up to 81% while the number of accumulation 220 mode particles increases by up to 246%. This points to enhanced Brownian coagulation among ultra-fine particles as a result of higher local concentrations near the emissions plume core.

Similarly, the mass distribution of Aitken mode particles decreases by up to 74% for high emissions spatial heterogeneity scenarios while a dramatic increase of up to 309% is observed for the accumulation mode mass concentration. Coagulation of smaller Aitken mode particles with accumulation mode particles contributes little change in the mass distribution as indicated 225 by a slight reduction in the Aitken mode mass concentration. This indicates that the increase in mass concentration in the accumulation mode is largely due to gas-particle partitioning, which will be discussed in detail in the next section.

### 3.3 Aerosol composition

Figure 5 shows cross sections in the x-y plane of aerosol ammonium, nitrate, and sulfate in the upper boundary layer ( $z \approx 900$  m) at  $t = 6$  h. The spatial heterogeneity  $\eta$  also displayed alongside each cross section. The spatial organization of both ammonium and nitrate closely matches the region of emissions in each scenario. This indicates that ammonium nitrate formation is occurring in the ammonia and nitric acid rich emissions plume, whereby the local gas phase concentration is in excess of the equilibrium condition thus allowing ammonia and nitric acid to partition into the aerosol. Farther away from the emissions plume, the concentration of ammonium and nitrate lowers as the equilibrium condition shifts to the gas phase.

Sulfate is far more uniform for each emissions scenario, resulting in lower values of spatial heterogeneity ( $\eta = 0.021$  for scenario 3) than either ammonium ( $\eta = 0.142$ ) or nitrate ( $\eta = 0.739$ ). This is because, while ammonia and nitric acid partition between the gas and aerosol phase according to their equilibrium condition, sulfuric acid has an extremely low volatility vapor pressure such that nearly all will exist in the aerosol phase as sulfate. Consequently, virtually no sulfate will re-enter the gas phase as sulfuric acid. This indicates that the spatial heterogeneity of the aerosol phase is determined by the volatility of aerosol species, whereby lower volatility species are more uniformly distributed while higher volatility compounds are more spatially heterogenous and concentrated near plumes with high concentrations of corresponding gas phase precursors.

Figure 6 shows vertical profiles of aerosol ammonium ( $\text{NH}_4^+$ ), nitrate ( $\text{NO}_3^-$ ), and sulfate ( $\text{SO}_4^{2-}$ ) for each emissions scenario. The uniform base case is indicated via the solid black line while scenarios are indicated by colored lines ranging from blue (low spatial heterogeneity) to light green (high spatial heterogeneity). These profiles represent the average concentration of aerosol species within each vertical level at the end of each simulation ( $t = 6$  h).

Sulfate concentrations are nearly uniform within the boundary layer and rapidly decrease above the entrainment zone due to little exchange between the free troposphere and the boundary layer. Sulfate concentrations decrease as the emissions spatial heterogeneity is increased. Note that for scenarios with high emissions spatial heterogeneity, the elevated concentration of reactive gas phase compounds in the emissions plume such as volatile organic compounds (VOCs) alongside sulfate's gas phase precursor  $\text{SO}_2$  results in greater effective competition for oxidation with OH. As a result, OH is rapidly depleted near the emissions plume, thereby reducing the potential for oxidation of  $\text{SO}_2$  to form  $\text{H}_2\text{SO}_4$  (which rapidly partitions into the aerosol phase as sulfate owing to its extremely low volatility vapor pressure). OH from outside the emissions plume is not mixed and entrained into the plume fast enough to restore its concentration (see Figure 2), thereby illustrating the impact of emissions spatial heterogeneity in chemically segregating reactive gas phase species OH and  $\text{SO}_2$ , and in altering the subsequent formation of sulfate through gas-particle partitioning.

Both ammonium and nitrate concentrations increase with height in the boundary layer due to the strong temperature dependence of ammonium nitrate formation. The abundance of nitrate depends on the availability of free ammonia, that is, ammonia in excess of what is required to neutralize sulfate as ammonium sulfate. In the lowest 500 m of the boundary layer, the concentration of  $\text{NH}_4^+$  decreases under high emissions spatial heterogeneity. The reduction in  $\text{NH}_4^+$  is likely a response to lower sulfate concentrations at higher emissions spatial heterogeneity. Sulfate rich particles are highly acidic which drives  $\text{NH}_3$  into

260 the aerosol to neutralize acidity by forming ammonium nitrate. Therefore, under high emissions spatial heterogeneity whereby sulfate concentrations are lowered, increased particle pH will decrease the partitioning of ammonia into the aerosol phase.

As emissions spatial heterogeneity increases, greater  $\text{NH}_4^+$  and  $\text{NO}_3^-$  form as ammonium nitrate in the aerosol phase towards the top of the boundary layer ( $z \sim 1.2 \text{ km}$  at  $t = 6 \text{ h}$ ). The decrease in sulfate concentrations for scenarios with high emissions spatial heterogeneity results in higher concentrations of free ammonia, thus allowing the formation of more ammonium nitrate.  
265 Note that in the uniform base case, almost no nitrate is formed due to the lack of free ammonium as nearly all  $\text{NH}_4^+$  is bound to sulfate as ammonium sulfate. This indicates the strong dependence of nitrate concentrations on the composition of the aerosol and the level of emissions spatial heterogeneity.

Figure 7 shows the size-resolved mass fraction of aerosols in the upper boundary layer ( $z \approx 800 \text{ m}$ ) for the initial condition and at the end of simulations ( $t = 6 \text{ h}$ ) for both the uniform base case and the maximally spatially heterogeneous emissions scenario, scenario 3. After 6 hours, a stark difference in composition is apparent between particles in the uniform base case and scenario 3. Under uniform, dilute emissions, particles are largely comprised of BC and organic carbon (OC) along with some sulfate. Particles that age under the spatially heterogeneous emissions of scenario 3 are dominated by nitrate, ammonium, and sulfate and jointly comprise between 50 to 80% of aerosol mass.  
270

The CCN activity of particles in the size range of 50-100 nm is largely dependent on their composition—in the presence of hygroscopic aerosol, the solute effect of Raoult’s Law lowers the critical supersaturation required for activation. Without the aid of hygroscopic material, small aerosol particles possess high critical supersaturations due to the Kelvin effect which increases vapor pressure over the particle surface due to its curvature. Figure 7 indicates that, for the uniform base case, particles in the size range of 50-100 nm are primarily composed of BC and OC (low hygroscopicity compounds) whereas sulfate, nitrate, and ammonium dominate the mass fraction in the same size range for the high emissions spatial heterogeneity scenario. This  
280 indicates that particles in the size range whose CCN activity hinges on aerosol composition are more hygroscopic under high emissions spatial heterogeneity scenarios and thus activate at lower supersaturations.

Figure 8 shows 2-dimensional number distributions  $n(D_p, \kappa)$  as a function of particle diameter  $D_p$  and particle hygroscopicity parameter  $\kappa$  in the upper boundary layer ( $z \approx 800 \text{ m}$ ). Particles are binned into a two-dimensional histogram by diameter (50 bins ranging from 10 nm to 1  $\mu\text{m}$ ) and bins are colored by their corresponding number concentration indicated by the  
285 colorbar. The initial condition is shown on the left whereby all particles possess the same composition and thus the same hygroscopicity. The inclusion of ammonium sulfate in the initial condition makes the particles moderately hygroscopic. On the right, the 2-dimensional size distribution is shown at the end of simulations ( $t = 6 \text{ h}$ ) for both the uniform base case and the maximally spatially heterogeneous scenario, scenario 3.

Two primary groupings of particles are noticeable for the uniform base case—a grouping of lower  $\kappa$  particles between  
290  $\kappa = 0$  and  $\kappa \approx 0.3$  alongside a grouping of particles with higher  $\kappa$  ranging from  $\kappa \approx 0.3$  to  $\kappa \approx 0.6$ . The grouping of lower  $\kappa$  particles correspond to carbonaceous primary aerosol which have not undergone significant aging in the form of coagulation and gas-particle partitioning which increase the fraction of hygroscopic compounds (such as sulfate, nitrate, and ammonium). The upper band of higher  $\kappa$  particles is shown to increase towards smaller particles, consistent with the elevated levels of sulfate observed in particles between 20–50 nm in the uniform base case shown in Figure 7.

295 By comparison to the uniform base case, the number distribution for scenario 3 indicates the presence of higher  $\kappa$  particles. For instance, the hygroscopicity of particles with diameter of 100 nm is in excess of  $\kappa > 0.6$  for scenario 3 (indicating highly hygroscopic particles), whereas  $\kappa$  only reaches up to 0.4 for 100 nm particles in the uniform base case. These findings show that spatially heterogeneous emissions can elevate the hygroscopicity of particles whose CCN activity is dependent on particle composition ( $D_p \sim 50\text{--}100\text{ nm}$ ).

300 Note that differences in the 2-dimensional number distributions with regard to  $\kappa$  between the uniform base case and scenario 3 can be attributed to the coupling between emissions spatial heterogeneity and sub-grid scale aerosol processes. As previously noted, the enhancement of coagulation in spatially heterogeneous emission plumes reduces the concentration of Aitken mode particles. This helps explain the absence of a grouping of low- $\kappa$  carbonaceous primary aerosol particles. Furthermore, enhancements to gas-particle partitioning due to spatially heterogeneous emissions are responsible for increasing the hygroscopicity of 305 particles. In particular, the formation of ammonium nitrate in scenario 3 due to reduced levels of sulfate and a corresponding increase in free ammonia elevate particle hygroscopicity.

### 3.4 CCN activity

Figure 9 shows vertical profiles of the CCN number concentration per kilogram of dry air for supersaturations  $S$  ranging from  $S = 0.1\%$  to  $S = 1.0\%$  and for each emissions scenario. Note that the ambient relative humidity (RH) in each simulation does 310 not exceed 100%—instead, reported CCN concentrations indicate the number of particles that would activate given the RH were raised to the specified supersaturation.

As noted previously, the coupling between emissions spatial heterogeneity and aerosol processes such as coagulation and gas-particle partitioning are responsible for altering the number, size, composition, and hygroscopicity of particles. These processes in turn modify the resulting CCN activity; however, the dominant processes contributing to changes in CCN activity 315 and the strength of effect vary with supersaturation.

At low supersaturations ( $S = 0.1\text{--}0.3\%$ ), CCN activity increases with emissions spatial heterogeneity in the upper boundary layer due to enhanced formation of ammonium nitrate in the cooler, sulfate poor environment. This elevates activation of ultrafine particles in the range of 50–100 nm due to the high hygroscopicity of ammonium nitrate.

At higher supersaturations ( $S = 0.6\text{--}1.0\%$ ), an increase in CCN activity in the upper boundary layer is still found for emissions scenarios with lower spatial heterogeneity, however, at high emissions heterogeneity (scenario 3), the number concentration is reduced. This effect is most prominent at the highest supersaturation ( $S = 1.0\%$ ), whereby the number concentration of CCN throughout the boundary layer is less than all other scenarios including the uniform base case. This phenomenon is due to the enhancement of coagulation by the emissions spatial heterogeneity and illustrates how coagulation has a competing effect 320 on CCN activity which dominates at high supersaturations. Note that small, non-hygroscopic particles possess high critical supersaturations. Additionally, the enhancement to coagulation for emissions scenarios with high spatial heterogeneity acts to efficiently remove smaller particles. Therefore, at sufficiently high supersaturation and emissions spatial heterogeneity, the negative effect on CCN activity due to coagulation will dominate the positive effect introduced by gas-particle partitioning of 325 hygroscopic material.

Figure 10 shows time vs. height plots of the percent difference between the CCN concentrations at each supersaturation level  
 330 and emissions scenario and the corresponding CCN concentrations in the uniform base case. Percent difference is calculated  
 as

$$\% \text{ difference} = 100 \times \left( \frac{\overline{[\text{CCN}]}(t, z, S)_{\text{Scenario}} - \overline{[\text{CCN}]}(t, z, S)_{\text{Base case}}}{\overline{[\text{CCN}]}(t, z, S)_{\text{Base case}}} \right), \quad (2)$$

where  $\overline{[\text{CCN}]}(t, z, S)_{\text{Scenario}}$  is the horizontally averaged concentration of CCN at time  $t$  and vertical level  $z$  that activate at  
 335 supersaturation  $S$  for the given emissions scenario and  $\overline{[\text{CCN}]}(t, z, S)_{\text{Base case}}$  is the horizontally averaged concentration of  
 CCN at time  $t$  and vertical level  $z$  that activate at supersaturation  $S$  for the uniform base case.

The greatest increase in CCN activity occurs for scenario 3, the highest spatial heterogeneity emissions scenario, at a  
 supersaturation of  $S = 0.3\%$  whereby CCN concentrations increase by upwards of 25% through  $t = 6$  h. Across each scenario,  
 the location of greatest increase in CCN activity grows with time due to boundary layer development. Moving down (higher  
 340 supersaturation) and to the right (higher emissions spatial heterogeneity) in Figure 10, the reduction in CCN activity due to the  
 enhancement of coagulation (see discussion of Figure 9 for a process-level description) manifests after approximately 5 hours  
 of simulation. Note that the increase in CCN activity coincides with the region where shallow cumulus and stratiform clouds  
 tend to form. As a result of the first indirect effect, the albedo of such clouds would be greater over regions with spatially  
 heterogeneous emissions of gas phase precursors and aerosols than over regions with low emissions heterogeneity.

### 3.5 Influence of ammonia on aerosol composition and CCN activity

345 We have shown that CCN activity is modulated by emissions spatial heterogeneity due to enhancements to coagulation and  
 the gas-particle partitioning of ammonia and nitric acid to form ammonium nitrate which elevates particle hygroscopicity. Furthermore,  
 the formation of ammonium nitrate is governed by the availability of free ammonia. To investigate the sensitivity of  
 changes in CCN activity due to the presence of ammonia in spatially heterogeneous emissions, a set of two additional simulations  
 350 were run for the uniform base case and scenario 3 in which the concentration of total ammonium ( $\text{NH}_3, \text{gas} + \text{NH}_4, \text{aerosol}$ )  
 is set to zero. Emissions of  $\text{NH}_3$  are also set to zero to ensure that total ammonium remains zero throughout each simulation.

Figure 11 shows vertical profiles of CCN concentrations in number of particles per kilogram of dry air at supersaturations  
 ranging from  $S = 0.1\%$  to  $S = 1.0\%$  and at  $t = 6$  h. Profiles for simulations containing ammonia are displayed as solid lines  
 while simulations without ammonia are shown as dashed lines. We find that, without ammonia, CCN concentrations at each  
 supersaturation level agree much closer. The peak of CCN concentrations in the upper boundary layer and at lower supersaturations  
 355 found for scenario 3 with ammonia is entirely absent. This underscores the significance of the coupling between spatially  
 heterogeneous emissions, their composition, and the formation of ammonium nitrate via gas-particle partitioning in altering  
 CCN activity, especially at lower supersaturations.

At higher supersaturations, particularly at  $S = 1.0\%$ , the reduction in CCN concentrations for scenario 3 without ammonia  
 relative to the corresponding uniform base case point to the enhancement of coagulation under spatially heterogeneous  
 360 emissions. Without the countervailing effect of gas-particle partitioning in increasing CCN activity due to ammonium nitrate

formation, the vertical profiles of the ammonia-free uniform base case and scenario 3 closely match each other, albeit with an offset for scenario 3 due to the enhancement of coagulation that shifts the number concentration lower by approximately 5%.

### 3.6 Influence of PBL wind on CCN activity

## 4 Conclusions

365 This study investigates the impacts of spatially heterogeneous emissions on aerosol properties in a convective boundary layer including CCN activity using a first-of-a-kind particle-resolved large-eddy simulation modeling framework, WRF-PartMC-MOSAIC-LES. This platform permits a process level analysis of the coupling between emissions spatial heterogeneity and concentration dependent aerosol processes such as coagulation and gas-particle partitioning. Emissions spatial heterogeneity is varied using numerous idealized scenarios and are compared against a base case of uniform emissions which acts as a proxy  
370 for coarser-resolved models whose grid resolution is insufficient to represent the underlying spatial heterogeneity of emissions.

Key aerosol processes including gas-particle partitioning and coagulation are impacted by emissions spatial heterogeneity, as we find significant changes to the sulfate-nitrate-ammonium system and an increased rate of coagulation under high emissions spatial heterogeneity scenarios. In particular, nitrate formation is shown to dramatically increase with emissions spatial heterogeneity; the local increase in nitric acid and ammonia concentrations near the emissions plume core shifts the equilibrium  
375 condition from the gas phase to allow ammonium nitrate formation in the aerosol phase.

Changes to aerosol processes have downstream effects on CCN activity. Furthermore, modifications by emissions spatial heterogeneity to coagulation and gas-particle partitioning result in competing effects on the concentration of CCN at a given supersaturation level. Coagulation removes smaller particles that activate at high supersaturations, resulting in a decrease in CCN activity at high supersaturations for scenarios with high emissions spatial heterogeneity. Conversely, coagulation is not as  
380 efficient at removing larger particles that activate at lower supersaturations and gas-particle partitioning results in an increase of highly hygroscopic compounds such as ammonium nitrate under high emissions spatial heterogeneity. As a result, CCN activity at lower supersaturations ( $S = 0.3\text{--}0.6\%$ ) increases by up to 25% in the upper boundary layer for emissions scenarios with high spatial heterogeneity.

The effect of emissions spatial heterogeneity on CCN activity is highly dependent on the composition of the aerosol and  
385 gas phase. Given the key contribution of ammonium nitrate formation in elevating CCN activity under highly spatially heterogeneous scenarios, the removal of ammonia decreases—or in some cases reverses—the trend between emissions spatial heterogeneity and CCN activity. Note that the treatment of nitrate formation in GCMs is often simplified by assuming equilibrium partitioning, or in other cases, nitrate in the aerosol phase is not modeled. This work underscores the importance of representing nitrate in GCM chemical mechanisms due to the strong coupling between emissions spatial heterogeneity, aerosol  
390 composition, and CCN activity. As model resolution continues to improve, it is essential for the representation of aerosol chemistry to advance alongside the representation of emissions spatial heterogeneity.

*Code availability.* TEXT

*Data availability.* TEXT

*Code and data availability.* TEXT

395 *Sample availability.* TEXT

*Video supplement.* TEXT

## **Appendix A**

### **A1**

*Author contributions.* TEXT

400 *Competing interests.* TEXT

*Disclaimer.* TEXT

*Acknowledgements.* TEXT

## References

- Brasseur, G. P., Barth, M., Kazil, J., Patton, E., and Wang, Y.: Segregation of Fast-Reactive Species in Atmospheric Turbulent Flow,  
405 https://doi.org/10.20944/preprints202305.0895.v1, 2023.
- Ching, J., Fast, J., West, M., and Riemer, N.: Metrics to quantify the importance of mixing state for CCN activity, *Atmospheric Chemistry and Physics*, 17, 7445–7458, https://doi.org/10.5194/acp-17-7445-2017, publisher: Copernicus GmbH, 2017.
- Crippa, P., Sullivan, R. C., Thota, A., and Pryor, S. C.: The impact of resolution on meteorological, chemical and aerosol properties in  
410 regional simulations with WRF-Chem, *Atmospheric Chemistry and Physics*, 17, 1511–1528, https://doi.org/10.5194/acp-17-1511-2017, publisher: Copernicus GmbH, 2017.
- Curtis, J. H., Riemer, N., and West, M.: A single-column particle-resolved model for simulating the vertical distribution of aerosol mixing state: WRF-PartMC-MOSAIC-SCM v1.0, *Geoscientific Model Development*, 10, 4057–4079, https://doi.org/10.5194/gmd-10-4057-  
2017, publisher: Copernicus GmbH, 2017.
- Curtis, J. H., Riemer, N., and West, M.: Explicit stochastic advection algorithms for the regional-scale particle-resolved atmospheric aerosol  
415 model WRF-PartMC (v1.0), *Geoscientific Model Development*, 17, 8399–8420, https://doi.org/10.5194/gmd-17-8399-2024, 2024.
- de Bruine, M., Krol, M., Vilà-Guerau de Arellano, J., and Röckmann, T.: Explicit aerosol–cloud interactions in the Dutch Atmospheric Large-Eddy Simulation model DALES4.1-M7, *Geoscientific Model Development*, 12, 5177–5196, https://doi.org/10.5194/gmd-12-5177-2019, publisher: Copernicus GmbH, 2019.
- Deardorff, J. W.: Stratocumulus-capped mixed layers derived from a three-dimensional model, *Boundary-Layer Meteorology*, 18, 495–527,  
420 https://doi.org/10.1007/BF00119502, 1980.
- Fierce, L., Riemer, N., and Bond, T. C.: When is cloud condensation nuclei activity sensitive to particle characteristics at emission?, *Journal of Geophysical Research: Atmospheres*, 118, 13,476–13,488, https://doi.org/10.1002/2013JD020608, \_eprint: https://onlinelibrary.wiley.com/doi/pdf/10.1002/2013JD020608, 2013.
- Fierce, L., Riemer, N., and Bond, T. C.: Explaining variance in black carbon’s aging timescale, *Atmospheric Chemistry and Physics*, 15,  
425 3173–3191, https://doi.org/10.5194/acp-15-3173-2015, publisher: Copernicus GmbH, 2015.
- Fierce, L., Yao, Y., Easter, R., Ma, P.-L., Sun, J., Wan, H., and Zhang, K.: Quantifying structural errors in cloud condensation nuclei activity from reduced representation of aerosol size distributions, *Journal of Aerosol Science*, 181, 106388, https://doi.org/10.1016/j.jaerosci.2024.106388, 2024.
- Forster, P., Storelvmo, T., Armour, K., Collins, W., Dufresne, J.-L., Frame, D., Lunt, D., Mauritsen, T., Palmer, M., Watanabe, M., Wild,  
430 M., and Zhang, H.: The Earth’s Energy Budget, Climate Feedbacks, and Climate Sensitivity, p. 923–1054, Cambridge University Press, Cambridge, United Kingdom and New York, NY, USA, https://doi.org/10.1017/9781009157896.009, 2021.
- Golaz, J., Van Roekel, L. P., Zheng, X., Roberts, A. F., Wolfe, J. D., Lin, W., Bradley, A. M., Tang, Q., Maltrud, M. E., Forsyth, R. M., Zhang, C., Zhou, T., Zhang, K., Zender, C. S., Wu, M., Wang, H., Turner, A. K., Singh, B., Richter, J. H., Qin, Y., Petersen, M. R., Mametjanov, A., Ma, P., Larson, V. E., Krishna, J., Keen, N. D., Jeffery, N., Hunke, E. C., Hannah, W. M., Guba, O., Griffin, B. M., Feng, Y., Engwirda, D., Di Vittorio, A. V., Dang, C., Conlon, L. M., Chen, C., Brunke, M. A., Bisht, G., Benedict, J. J., Asay-Davis, X. S., Zhang, Y., Zhang, M., Zeng, X., Xie, S., Wolfram, P. J., Vo, T., Veneziani, M., Tesfa, T. K., Sreepathi, S., Salinger, A. G., Reeves Eyre, J. E. J., Prather, M. J., Mahajan, S., Li, Q., Jones, P. W., Jacob, R. L., Huebler, G. W., Huang, X., Hillman, B. R., Harrop, B. E., Foucar, J. G., Fang, Y., Comeau, D. S., Caldwell, P. M., Bartoletti, T., Balaguru, K., Taylor, M. A., McCoy, R. B., Leung, L. R., and Bader, D. C.: The DOE  
435

440 14, e2022MS003 156, <https://doi.org/10.1029/2022MS003156>, 2022.

Gustafson Jr., W. I., Qian, Y., and Fast, J. D.: Downscaling aerosols and the impact of neglected subgrid processes on direct aerosol radiative forcing for a representative global climate model grid spacing, *Journal of Geophysical Research: Atmospheres*, 116, <https://doi.org/10.1029/2010JD015480>, 2011.

445 Kaser, L., Karl, T., Yuan, B., Mauldin III, R. L., Cantrell, C. A., Guenther, A. B., Patton, E. G., Weinheimer, A. J., Knotz, C., Orlando, J., Emmons, L., Apel, E., Hornbrook, R., Shertz, S., Ullmann, K., Hall, S., Graus, M., de Gouw, J., Zhou, X., and Ye, C.: Chemistry-turbulence interactions and mesoscale variability influence the cleansing efficiency of the atmosphere, *Geophysical Research Letters*, 42, 10,894–10,903, <https://doi.org/10.1002/2015GL066641>, \_eprint: <https://onlinelibrary.wiley.com/doi/pdf/10.1002/2015GL066641>, 2015.450 Kokkola, H., Korhonen, H., Lehtinen, K. E. J., Makkonen, R., Asmi, A., Järvenoja, S., Anttila, T., Partanen, A.-I., Kulmala, M., Järvinen, H., Laaksonen, A., and Kerminen, V.-M.: SALSA — a Sectional Aerosol module for Large Scale Applications, *Atmospheric Chemistry and Physics*, 8, 2469–2483, <https://doi.org/10.5194/acp-8-2469-2008>, publisher: Copernicus GmbH, 2008.

Kurppa, M., Hellsten, A., Roldin, P., Kokkola, H., Tonttila, J., Auvinen, M., Kent, C., Kumar, P., Maronga, B., and Järvi, L.: Implementation of the sectional aerosol module SALSA2.0 into the PALM model system 6.0: model development and first evaluation, *Geoscientific Model Development*, 12, 1403–1422, <https://doi.org/10.5194/gmd-12-1403-2019>, publisher: Copernicus GmbH, 2019.

455 Lin, G., Qian, Y., Yan, H., Zhao, C., Ghan, S. J., Easter, R., and Zhang, K.: Quantification of marine aerosol subgrid variability and its correlation with clouds based on high-resolution regional modeling, *Journal of Geophysical Research: Atmospheres*, 122, 6329–6346, <https://doi.org/10.1002/2017JD026567>, 2017.

Ma, P.-L., Rasch, P. J., Wang, M., Wang, H., Ghan, S. J., Easter, R. C., Gustafson Jr., W. I., Liu, X., Zhang, Y., and Ma, H.-Y.: How does increasing horizontal resolution in a global climate model improve the simulation of aerosol-cloud interactions?, *Geophysical Research Letters*, 42, 5058–5065, <https://doi.org/10.1002/2015GL064183>, \_eprint: <https://onlinelibrary.wiley.com/doi/pdf/10.1002/2015GL064183>, 2015.

460 Mohebalhojeh, M., Frederick, S., Riemer, N., and West, M.: A Measure of Spatial Heterogeneity, (in prep), 2024.

Ouwersloot, H. G., Vilà-Guerau de Arellano, J., van Heerwaarden, C. C., Ganzeveld, L. N., Krol, M. C., and Lelieveld, J.: On the segregation of chemical species in a clear boundary layer over heterogeneous land surfaces, *Atmospheric Chemistry and Physics*, 11, 10 681–10 704, <https://doi.org/10.5194/acp-11-10681-2011>, publisher: Copernicus GmbH, 2011.

465 Qian, Y., Gustafson, W. I. J., and Fast, J. D.: An investigation of the sub-grid variability of trace gases and aerosols for global climate modeling, *Atmospheric Chemistry and Physics*, 10, 6917–6946, <https://doi.org/10.5194/acp-10-6917-2010>, publisher: Copernicus GmbH, 2010.

Riemer, N., West, M., Zaveri, R. A., and Easter, R. C.: Simulating the evolution of soot mixing state with a particle-resolved aerosol model, *Journal of Geophysical Research: Atmospheres*, 114, <https://doi.org/10.1029/2008JD011073>, 2009.

470 Skamarock, C., Klemp, B., Dudhia, J., Gill, O., Barker, D., Duda, G., Huang, X.-y., Wang, W., and Powers, G.: A Description of the Advanced Research WRF Version 3, <https://doi.org/10.5065/D68S4MVH>, 2008.

Tilmes, S., Mills, M. J., Zhu, Y., Bardeen, C. G., Vitt, F., Yu, P., Fillmore, D., Liu, X., Toon, B., and Deshler, T.: Description and performance of a sectional aerosol microphysical model in the Community Earth System Model (CESM2), *Geoscientific Model Development*, 16, 6087–6125, <https://doi.org/10.5194/gmd-16-6087-2023>, publisher: Copernicus GmbH, 2023.

- 475 Tonttila, J., Maalick, Z., Raatikainen, T., Kokkola, H., Kühn, T., and Romakkaniemi, S.: UCLALES-SALSA v1.0: a large-eddy model with interactive sectional microphysics for aerosol, clouds and precipitation, *Geoscientific Model Development*, 10, 169–188, <https://doi.org/10.5194/gmd-10-169-2017>, publisher: Copernicus GmbH, 2017.
- Vignati, E., Wilson, J., and Stier, P.: M7: An efficient size-resolved aerosol microphysics module for large-scale aerosol transport models, *Journal of Geophysical Research: Atmospheres*, 109, <https://doi.org/10.1029/2003JD004485>, \_eprint: 480 <https://onlinelibrary.wiley.com/doi/pdf/10.1029/2003JD004485>, 2004.
- Weigum, N., Schutgens, N., and Stier, P.: Effect of aerosol subgrid variability on aerosol optical depth and cloud condensation nuclei: implications for global aerosol modelling, *Atmospheric Chemistry and Physics*, 16, 13 619–13 639, <https://doi.org/10.5194/acp-16-13619-2016>, publisher: Copernicus GmbH, 2016.
- Zaveri, R. A. and Peters, L. K.: A new lumped structure photochemical mechanism for large-scale applications, *Journal of Geophysical Research: Atmospheres*, 104, 30 387–30 415, <https://doi.org/10.1029/1999JD900876>, 1999.
- Zaveri, R. A., Easter, R. C., and Peters, L. K.: A computationally efficient Multicomponent Equilibrium Solver for Aerosols (MESA), *Journal of Geophysical Research: Atmospheres*, 110, <https://doi.org/10.1029/2004JD005618>, 2005a.
- Zaveri, R. A., Easter, R. C., and Wexler, A. S.: A new method for multicomponent activity coefficients of electrolytes in aqueous atmospheric aerosols, *Journal of Geophysical Research: Atmospheres*, 110, <https://doi.org/10.1029/2004JD004681>, \_eprint: 490 <https://onlinelibrary.wiley.com/doi/pdf/10.1029/2004JD004681>, 2005b.
- Zaveri, R. A., Easter, R. C., Fast, J. D., and Peters, L. K.: Model for Simulating Aerosol Interactions and Chemistry (MOSAIC), *Journal of Geophysical Research: Atmospheres*, 113, <https://doi.org/10.1029/2007JD008782>, 2008.
- Zaveri, R. A., Barnard, J. C., Easter, R. C., Riemer, N., and West, M.: Particle-resolved simulation of aerosol size, composition, mixing state, and the associated optical and cloud condensation nuclei activation properties in an evolving urban plume, *Journal of Geophysical Research: Atmospheres*, 115, <https://doi.org/10.1029/2009JD013616>, 2010.
- Zaveri, R. A., Easter, R. C., Singh, B., Wang, H., Lu, Z., Tilmes, S., Emmons, L. K., Vitt, F., Zhang, R., Liu, X., Ghan, S. J., and Rasch, P. J.: Development and Evaluation of Chemistry-Aerosol-Climate Model CAM5-Chem-MAM7-MOSAIC: Global Atmospheric Distribution and Radiative Effects of Nitrate Aerosol, *Journal of Advances in Modeling Earth Systems*, 13, e2020MS002346, <https://doi.org/10.1029/2020MS002346>, \_eprint: <https://onlinelibrary.wiley.com/doi/pdf/10.1029/2020MS002346>, 2021.

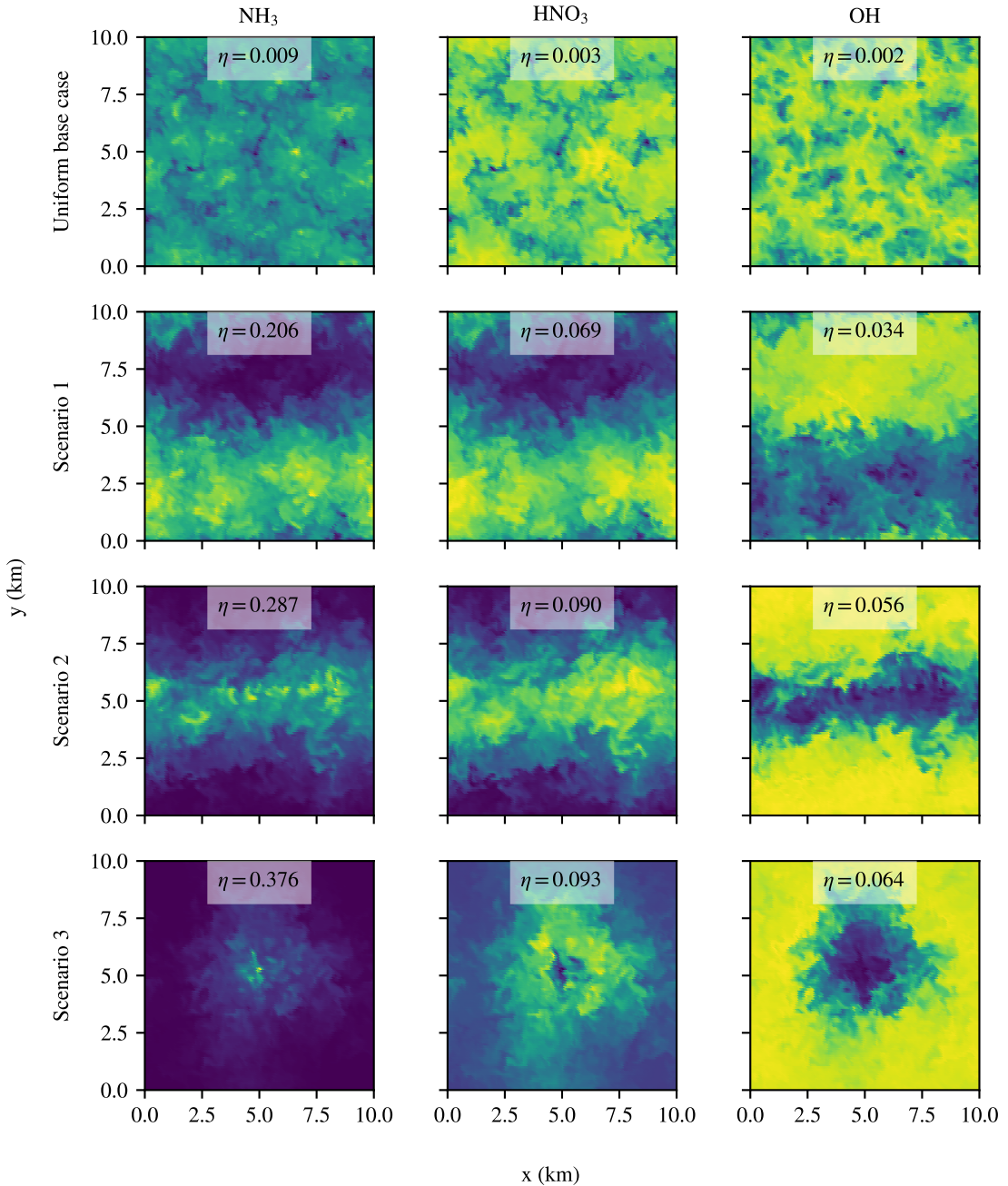


**Figure 2.** Cross sections in the x-y plane of gas phase species  $\text{NH}_3$  (left column),  $\text{HNO}_3$  (center column), and  $\text{OH}$  (right column). Cross sections are shown at a height of approximately  $z \approx 900$  m and at  $t = 6$  h. Rows are organized by emissions scenario ranging from the uniform base case to scenario 3. Color shading indicates the intensity of concentrations for each species and is normalized by the maximum and minimum concentration observed in each cross section. The value of the spatial heterogeneity metric  $\eta$  is displayed alongside each cross section plot.

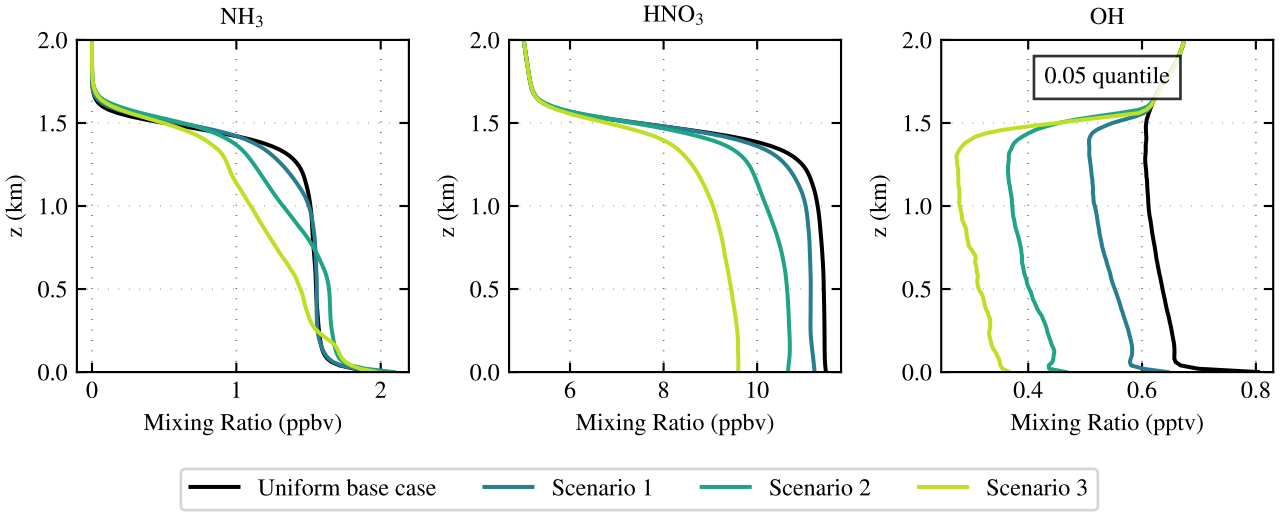


**Figure 3.** Vertical profiles of gas phase species  $\text{NH}_3$  (left),  $\text{HNO}_3$  (center), and  $\text{OH}$  (right) at  $t = 6$  h. For  $\text{NH}_3$  (left) and  $\text{HNO}_3$ , the mean value is displayed at each vertical level. For  $\text{OH}$ , the 5th percentile at each vertical level is shown to indicate the local changes to the  $\text{OH}$  concentration near the emissions plume. Values for the uniform base case are shown as a solid black line while emissions scenarios 1–3 are shown as colored solid lines.

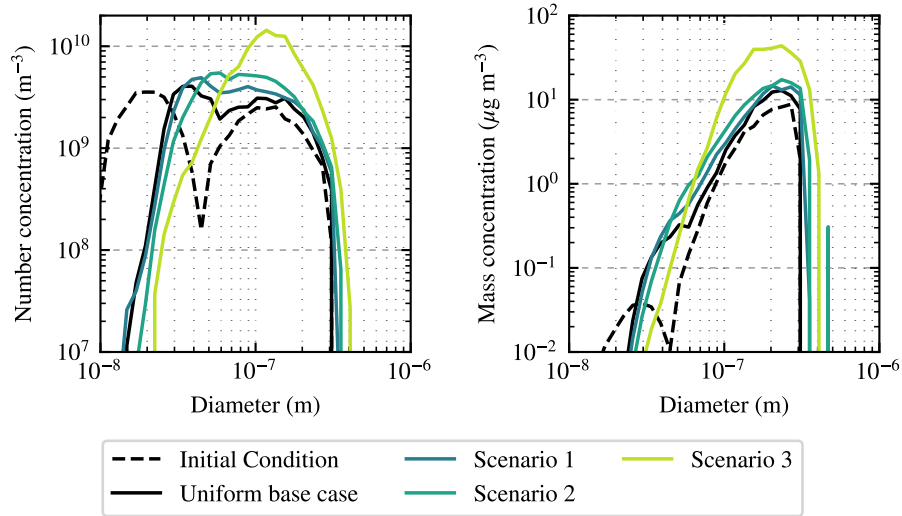


**Figure 4.** Number (left) and mass (right) distributions for each emissions scenario in the upper boundary layer ( $z = 800$  m) and  $t = 6$  h. The initial condition is shown as the dashed black line. Values for the uniform base case are shown as a solid black line while emissions scenarios 1–3 are shown as colored solid lines.

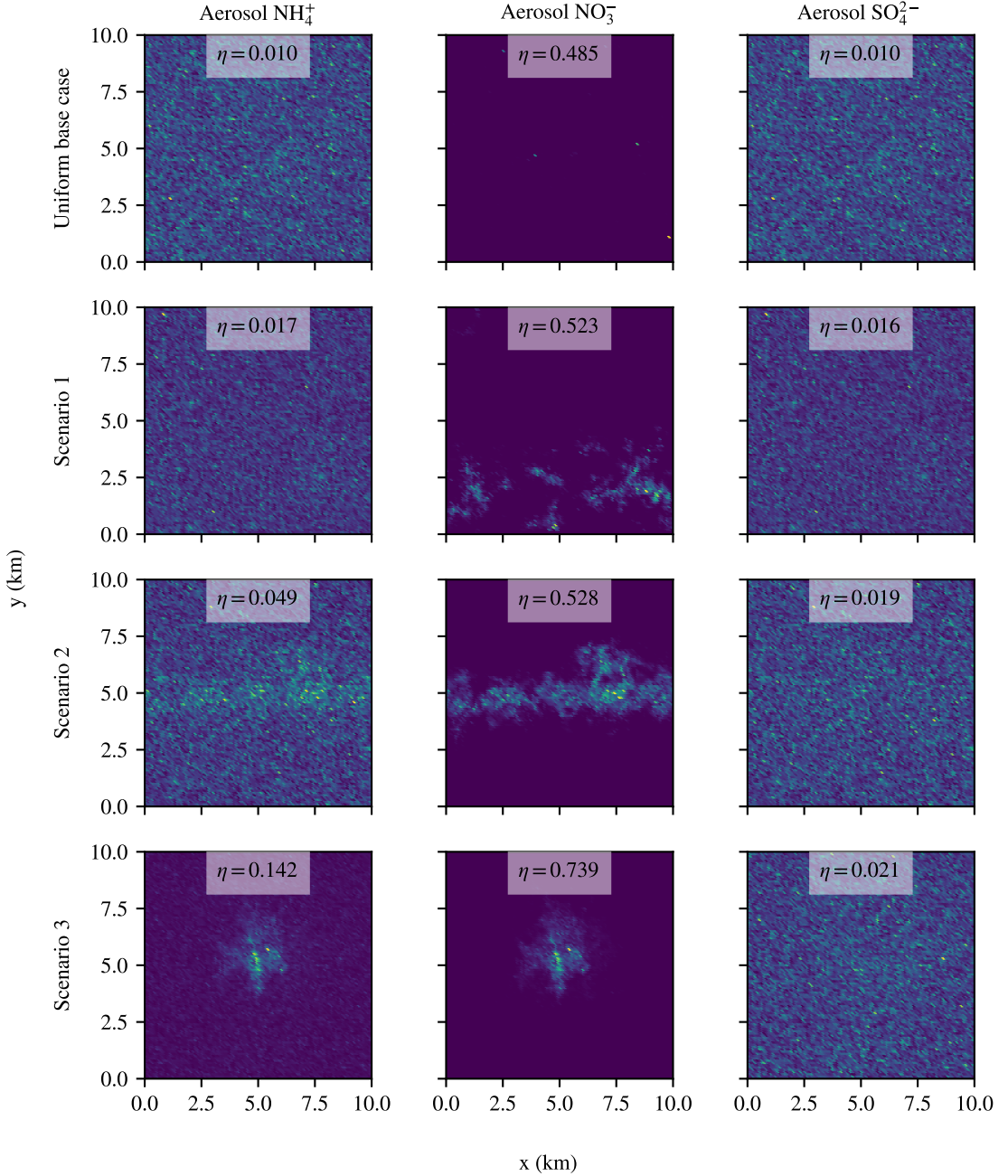


**Figure 5.** Cross sections in the x-y plane of aerosol species  $\text{NH}_4^+$  (left column),  $\text{NO}_3^-$  (center column), and  $\text{SO}_4^{2-}$  (right column). Cross sections are shown at a height of approximately  $z \approx 900$  m and at  $t = 6$  h. Rows are organized by emissions scenario ranging from the uniform base case to scenario 3. Color shading indicates the intensity of concentrations for each species and is normalized by the maximum and minimum concentration observed in each cross section. The value of the spatial heterogeneity metric  $\eta$  is displayed alongside each cross section plot.

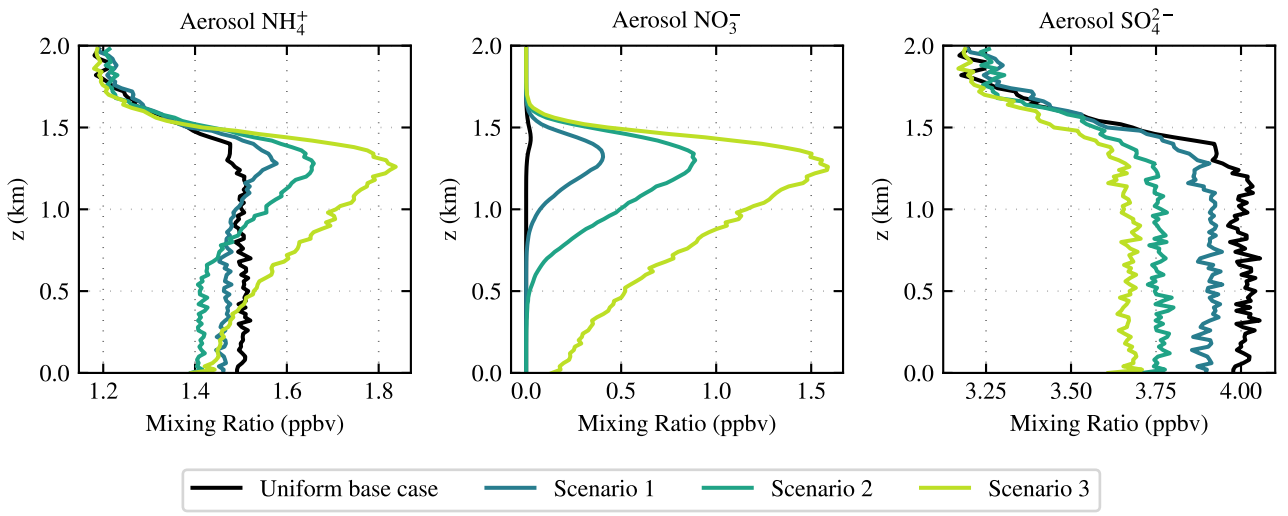


**Figure 6.** Vertical profiles of aerosol species  $\text{NH}_4^+$  (left),  $\text{NO}_3^-$  (center), and  $\text{SO}_4^{2-}$  (right) at  $t = 6$  h and in parts per billion by volume (ppbv). For each compound, the mean value is displayed at each vertical level. Values for the uniform base case are shown as a solid black line while emissions scenarios 1–3 are shown as colored solid lines.

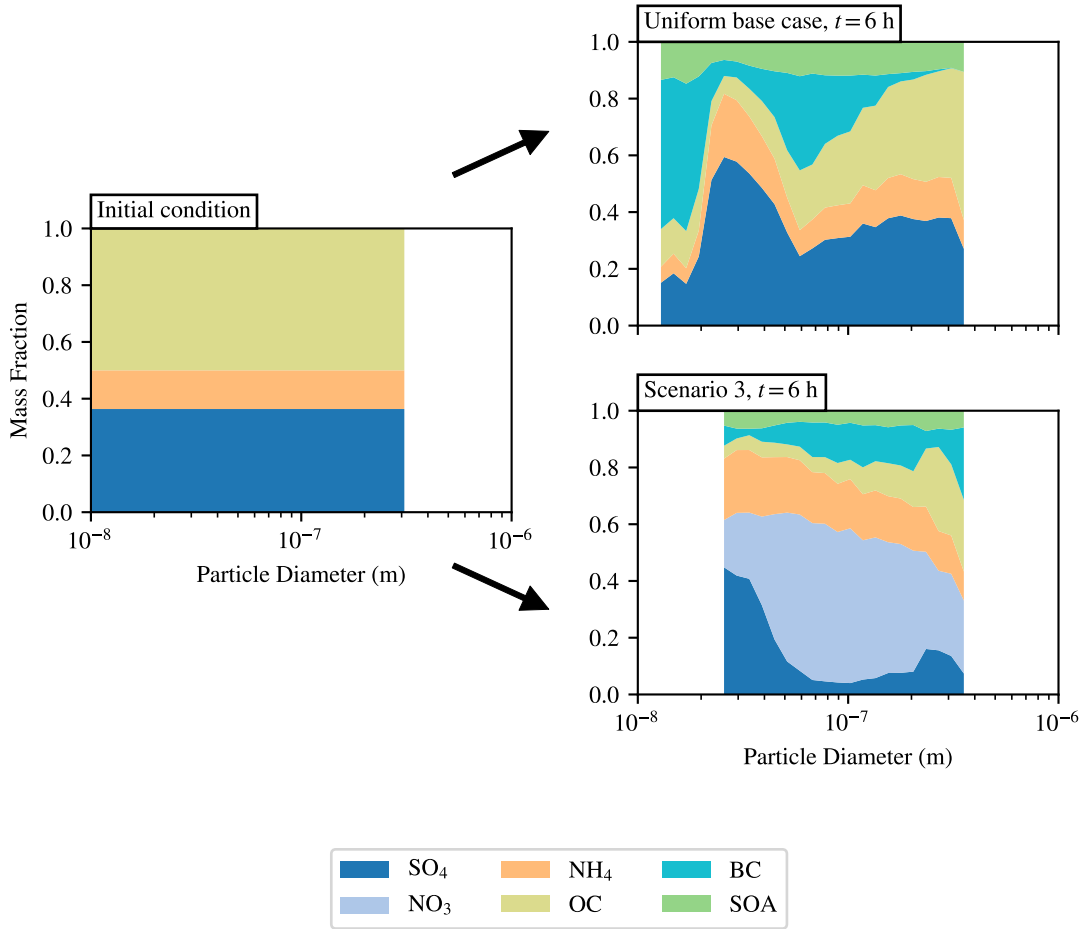


**Figure 7.** Speciated mass fraction as a function of particle diameter for emission scenario extremes. The initial condition is shown on the left, indicating that aerosol begin as an equal mixture of OC and ammonium sulfate. On the right, emissions scenarios with minimum spatial heterogeneity (top, uniform base case) and maximum spatial heterogeneity (bottom, scenario 3) are shown after 6 hours.

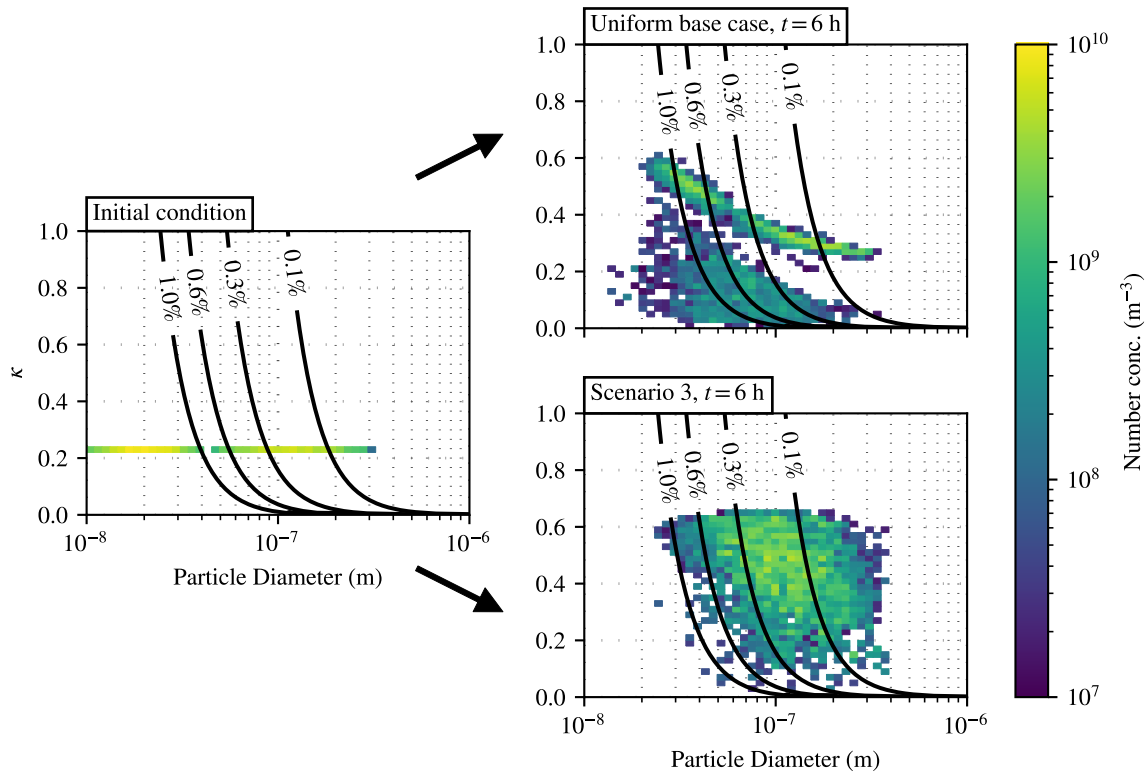


**Figure 8.** 2-dimensional number distributions  $n(D_p, \kappa)$  for emission scenario extremes. The initial condition is shown on the left, indicating that all aerosol begin as internally mixed particles with uniform  $\kappa$ . On the right, emissions scenarios with minimum spatial heterogeneity (top, uniform base case) and maximum spatial heterogeneity (bottom, scenario 3) are shown after 6 hours. Cell coloring indicates particle number concentration. Black solid contours indicate supersaturation in %. Particles to the right of a contour line activate at the indicated supersaturation.

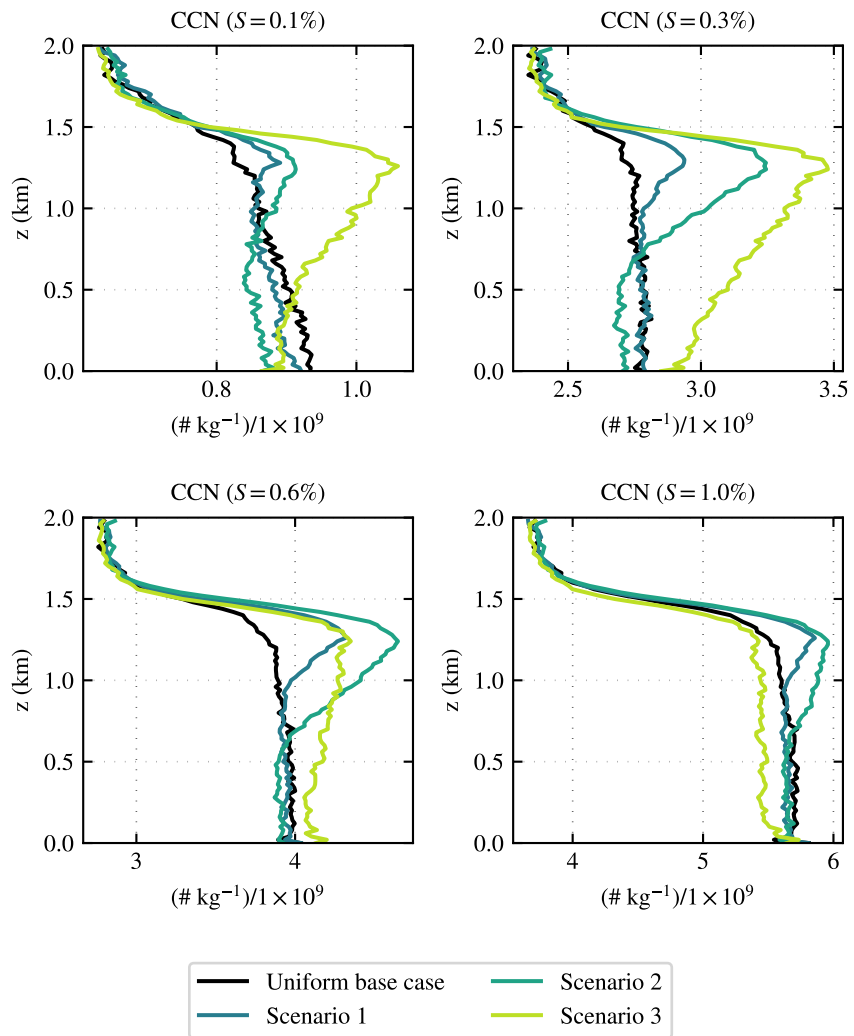


**Figure 9.** Vertical profiles for CCN concentrations activating at supersaturations  $S = 0.1, 0.3, 0.6, 1.0\%$  and at  $t = 6$  h. Concentrations are displayed in number of CCN per kilogram of dry air and are scaled by a factor of  $1 \times 10^{-9}$ . Values for the uniform base case are shown as a solid black line while emissions scenarios 1–3 are shown as colored solid lines.

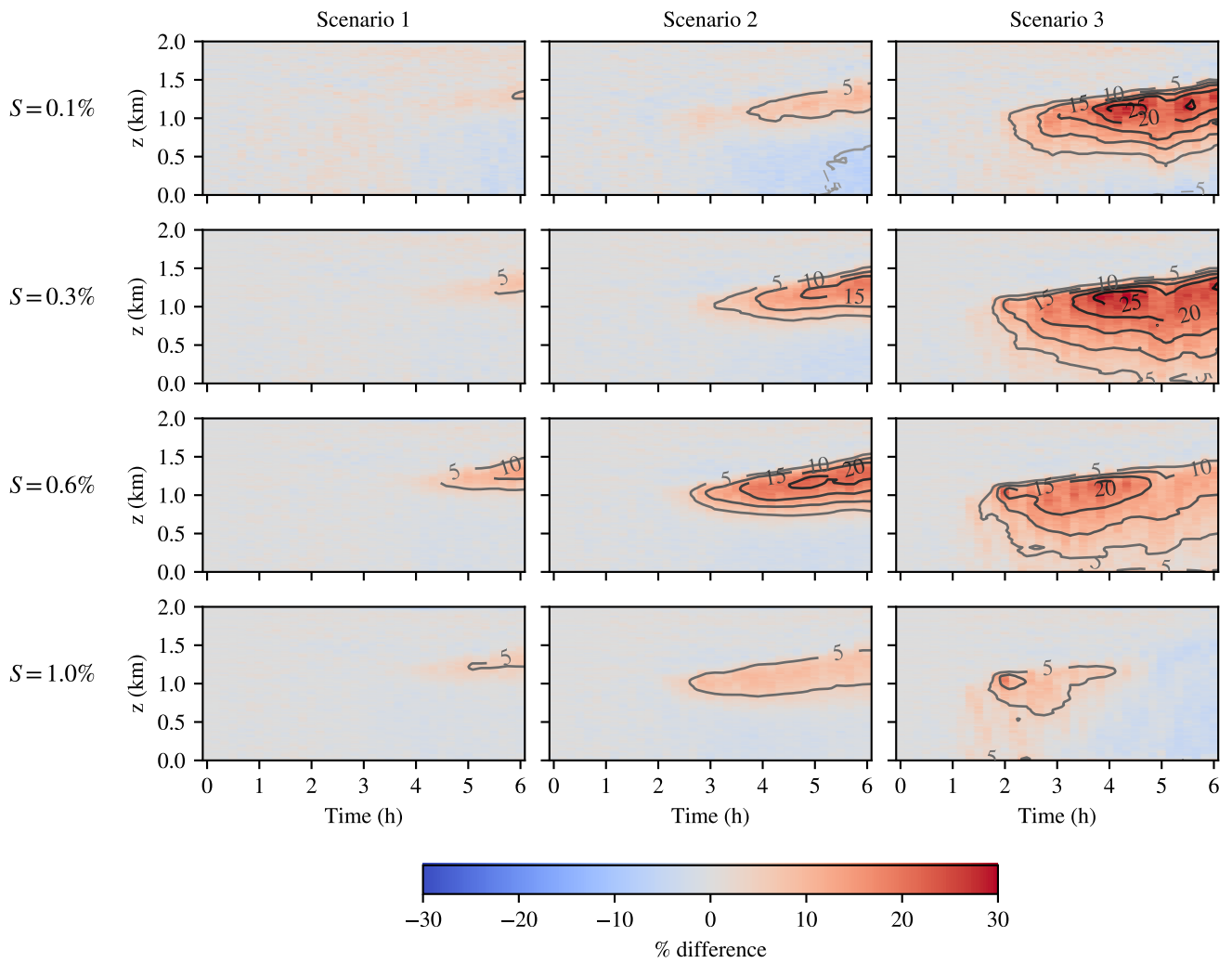


**Figure 10.** Time-height plots for the percent difference between CCN concentrations in the uniform base case and each emissions scenario and supersaturation level. Scenarios are organized by column. The supersaturation of CCN activation is organized by row. Red indicates an increase in CCN relative to the base case while blue indicates a reduction in CCN concentrations. Contour lines indicating regions of constant percent difference are drawn on each panel in increments of 5%.

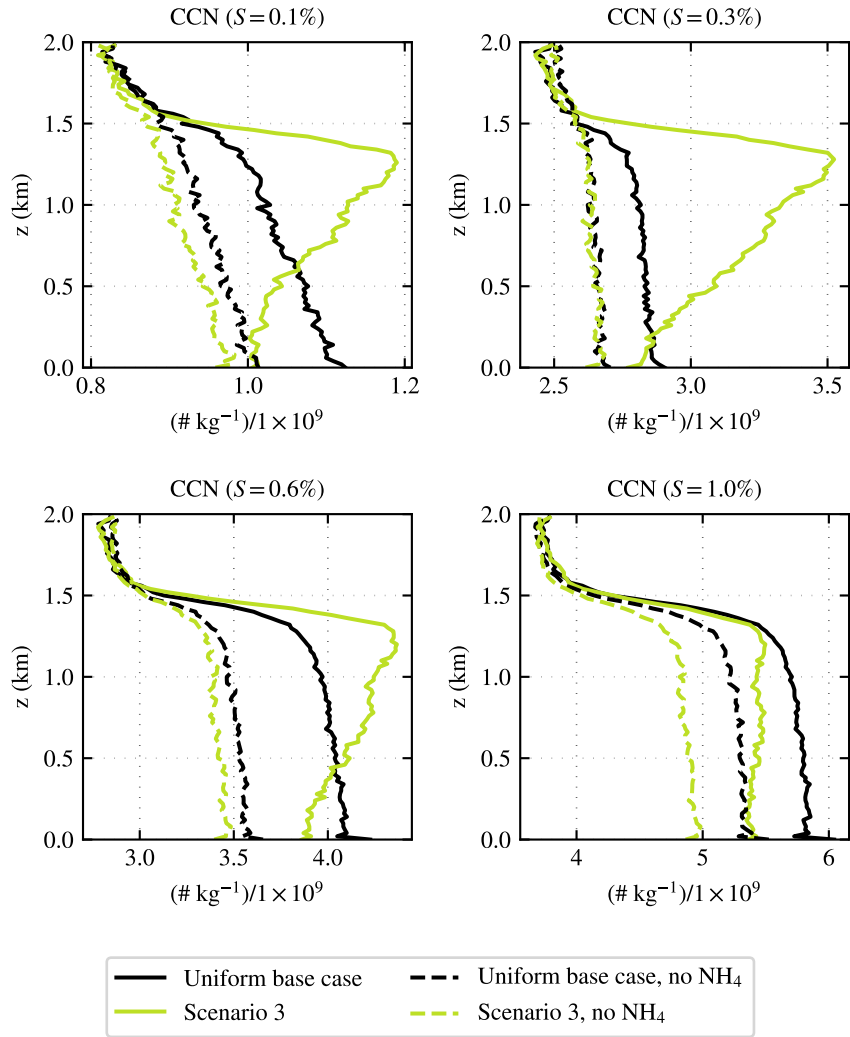


**Figure 11.** Vertical profiles for CCN concentrations in ammonia-free simulations that activate at supersaturations  $S = 0.1, 0.3, 0.6, 1.0\%$  and at  $t = 6$  h. Concentrations are displayed in number of CCN per kilogram of dry air and are scaled by a factor of  $1 \times 10^{-9}$ . Profiles for scenarios with ammonia are shown as solid lines while scenarios without ammonia are displayed as dashed lines for the uniform base case (black) and scenario 3 (chartreuse).